

Computation of Flow Pressure Fields from Magnetic Resonance Velocity Mapping

Guang-Zhong Yang, Philip J. Kilner, Nigel B. Wood, S. Richard Underwood, David N. Firmin

Magnetic resonance phase velocity mapping has unrivalled capacities for acquiring *in vivo* multi-directional blood flow information. In this study, the authors set out to derive both spatial and temporal components of acceleration, and hence differences of pressure in a flow field using cine magnetic resonance velocity data. An efficient numerical algorithm based on the Navier-Stokes equations for incompressible Newtonian fluid was used. The computational approach was validated with *in vitro* flow phantoms. This work aims to contribute to a better understanding of cardiovascular dynamics and to serve as a basis for investigating pulsatile pressure/flow relationships associated with normal and impaired cardiovascular function.

Key words: hemodynamics; pressure distributions; MR velocity imaging.

INTRODUCTION

The dynamics of blood flow through arteries are complex. Several distinct but interacting fluid mechanical factors contribute to pressures of blood at given locations and instants in the system. According to Newton's laws of motion, wherever fluid is subjected to momentum change, forces must be involved, which manifest as gradients of pressure. It is with this aspect of pressure, which we refer to as *flow pressure*, that we are concerned principally in this study. Regions of acceleration and deceleration of blood are associated with gradients of flow pressure. The magnitudes and spatio-temporal distributions of differences in flow pressure across blood masses contained by heart chambers and large vessels still have to be determined, both in healthy subjects and in patients with abnormal cardiovascular function. The proposed noninvasive approach provides access to this relatively unexplored aspect of pathophysiology.

In clinical cardiology, a modification of Bernoulli's equation has been used widely for estimation of pressure

differences across stenotic orifices from one-dimensional (1D) velocity data acquired by Doppler ultrasound (1, 2, 3, 4). While a reasonably good correlation has been achieved between the estimated results and actual measurements of pressure difference across stenoses, extension of the technique to other situations is limited by the inapplicability of Bernoulli's equation to unsteady flow. This limitation motivated us to approach the problem through the Navier-Stokes equations as they are recognized as a complete description of the mechanics of simple fluids.

The basic form of the Navier-Stokes equations, which are derived from considering the conservation of momentum in a control volume, can be represented as:

$$-\frac{\partial p}{\partial x_i} = \rho \frac{\partial u_i}{\partial t} + \rho \left(u_1 \frac{\partial u_i}{\partial x_1} + u_2 \frac{\partial u_i}{\partial x_2} + u_3 \frac{\partial u_i}{\partial x_3} \right) - \mu \left(\frac{\partial^2}{\partial x_1^2} + \frac{\partial^2}{\partial x_2^2} + \frac{\partial^2}{\partial x_3^2} \right) u_i - f_i \quad (i = 1, 2, 3) \quad [1]$$

with x_i ($i = 1, 2, 3$) representing the three orthogonal axes in space and u_i their corresponding velocity components. In Eq. [1], μ is the coefficient of viscosity, and ρ is the density of the fluid. Variables f_i ($i = 1, 2, 3$) represent the body force components along x_i . The above equations in fact represent the contribution to the momentum balance of the pressure force, transient and convective inertia, viscous resistance, and body force, i.e.,

$$\text{Pressure Force} = \text{Transient Inertia} + \text{Convective Inertia} - \text{Viscous Resistance} - \text{Body Force}.$$

The term *body force* refers to forces, such as gravity, acting directly on the fluid mass. Use of Eq. [1] for an incompressible fluid is commonly coupled with the divergence-free condition that provides local continuity or conservation of mass within the fluid region, and with the compatibility condition that ensures the global conservation of mass to obviate the effects of incremental errors introduced by numerical algorithms (5). Given velocity distribution $\mathbf{u} = (u_1, u_2, u_3)$ and body force $\mathbf{f} = (f_1, f_2, f_3)$ (notice that within the fluid the only body force present is gravity), the pressure gradient and thus the pressure, relative to an integration constant, can be calculated. The SI unit for pressure is pascal (Pa), which corresponds to newtons per square meter (N/m^2). In clinical settings, however, millimeters of mercury (mm Hg) are commonly used for recording pressure values.

MRM 36:520-526 (1996)

From the Magnetic Resonance Unit, Royal Brompton Hospital, London, United Kingdom.

Address correspondence to: G. Z. Yang, Ph.D., Magnetic Resonance Unit, Royal Brompton Hospital, 30 Brompton Street, London SW3 6NP, United Kingdom.

Received August 14, 1995; revised November 30, 1995; accepted January 3, 1996.

1996 SMR Young Investigators' Rabi Award Winner

This work was supported by the Coronary Artery Disease Research Association (CORDA) and the British Heart Foundation.

0740-3194/96 \$3.00

Copyright © 1996 by Williams & Wilkins

All rights of reproduction in any form reserved.

MATERIALS AND METHODS

MR Flow Data Acquisition

The velocity data used for this study were acquired using a Picker International Vista MR machine operating at 0.5 T with modified gradient coils and driven by a SMIS (Surrey Medical Imaging Systems, Ltd.) imaging console. Cine phase shift velocity mapping was performed using a gradient echo velocity sequence with an echo time of 14 ms. The slice thickness used was 10 mm and the field of view was 30 or 40 cm. The images were reconstructed on a 256×256 matrix from the average of 2×128 phase-encoding steps. For *in vivo* studies, 16 cine frames were acquired for each directional velocity map and were gated from the onset of the ECG (electrocardiogram) R wave.

Image Segmentation

Before pressure distribution calculation, velocity image segmentation was required to delineate the flow region and its corresponding boundaries. This process was performed interactively using the magnitude images associated with the velocity data to recognize anatomical structures. This step created a region mask, which was then used to register with the flow images so that the fluid region, denoted as Ω_F , and its corresponding boundary, denoted as $\partial\Omega_F$, required for pressure calculation, could be defined. A fully automatic segmentation approach was attempted, but with limited success for complicated regions.

Pressure Distribution Calculation

It can be seen from Eq. [1] that the pressure gradient $\nabla p = (p_{x_1}, p_{x_2}, p_{x_3})$, where $p_{x_i} \equiv \partial p / \partial x_i$ can be calculated directly from the given velocity data. Thereafter, an integration step is required to derive pressure from ∇p within the flow region. Given a reference pressure at position $(x_{1(0)}, x_{2(0)}, x_{3(0)})$, one can recover the relative pressure $p(x_1, x_2, x_3)$ by integrating along an arbitrary path such that

$$p(x_1, x_2, x_3) = p(x_{1(0)}, x_{2(0)}, x_{3(0)}) + \int_{(x_{1(0)}, x_{2(0)}, x_{3(0)})}^{(x_1, x_2, x_3)} (p_{x_1} dx_1 + p_{x_2} dx_2 + p_{x_3} dx_3). \quad [2]$$

In practice, however, this integration step can be troublesome because of noise presented within the original flow signal and the result might depend on the path chosen. A more practical solution to the problem is to take the least-squares method (6) and use the pressure Poisson equation to derive a consistent pressure distribution from ∇p . This is the approach that we have taken. A comparable approach to pressure estimation was used by Song *et al.* (7), who derived velocity information from analysis of ultrafast computed tomography (CT) images. In this paper, however, we adopt a simple yet effective iterative method for deriving pressure by which certain difficulties of the numerical methods described in (7) can be avoided.

Denote p_c as the final pressure distribution that is to be found. We seek to solve for p_c so that the gradient of p_c within Ω_F is as close as possible to the pressure gradient

∇p derived directly from the original velocity data. The problem can thus be formulated as follows and we aim to find p_c so that the error

$$\iiint_{\Omega_F} \sum_{i=1}^3 \left(\frac{\partial p_c}{\partial x_i} - p_{x_i} \right)^2 dx_1 dx_2 dx_3 \quad [3]$$

is minimized. According to the theory of calculus of variations (8), the Euler equation corresponding to the above integral is in the form of:

$$\nabla^2 p_c = \sum_{i=1}^3 \left(\frac{\partial p_{x_i}}{\partial x_i} \right), \quad \text{within } \Omega_F \quad [4]$$

In Eq. [4] the term ∇^2 is the Laplacian operator.

Before we proceed, however, we also need to know what to do about the boundary $\partial\Omega_F$ of Ω_F over which Eq. [4] is to be solved. The natural boundary condition (5) for an integral of the form shown in Eq. [3] is

$$\nabla p_c \cdot \mathbf{n} = \nabla p \cdot \mathbf{n}, \quad \text{on } \partial\Omega_F \quad [5]$$

in which \mathbf{n} is the outward normal vector on $\partial\Omega_F$. It, in essence, states that the normal derivative of the desired pressure distribution must equal the estimate of the normal derivative obtained from the data.

Numerical Algorithm

The Poisson equation described in Eq. [4] can be solved in many ways. For irregular flow region Ω_F , one of the most common approaches is to use lexicographic ordering, and the desired pressure distribution is solved through matrix manipulations. Although the matrices are mainly band-limited, their size can become extremely large and the amount of calculation involved is formidable, and thus impractical in our case. To circumvent this problem, an iterative scheme that incorporates a special property of the discretized Laplacian operator was used (9). In discrete form, the Laplacian operator can be represented as

$$\nabla^2 p_{c(i,j)} = \lambda (\bar{p}_{c(i,j)} - p_{c(i,j)}) \quad [6]$$

where λ is a constant depending on the differential mask that is used, and \bar{p} is the local average of p . The calculation of local averages will be dependent upon the chosen discretization scheme, and for a 3×3 area when only neighbors in the x_1 and x_2 directions are considered (four-neighborhood) it becomes

$$\bar{p}_{c(i,j)} = \frac{1}{4} (p_{c(i-1,j)} + p_{c(i+1,j)} + p_{c(i,j-1)} + p_{c(i,j+1)}). \quad [7]$$

When all eight neighbors are considered we have:

$$\begin{aligned} \bar{p}_{c(i,j)} = & \frac{1}{5} (p_{c(i+1,j)} + p_{c(i-1,j)} + p_{c(i,j+1)} + p_{c(i,j-1)}) \\ & + \frac{1}{20} (p_{c(i+1,j+1)} + p_{c(i+1,j-1)} + p_{c(i-1,j-1)} + p_{c(i-1,j+1)}) \end{aligned} \quad [8]$$

In this study, however, only Eq. [7] was used in the calculation. The final iterative process can now be formulated as follows:

$$p_c^{(k+1)} = \bar{p}_c^{(k)} - \frac{1}{\lambda} \sum_{i=1}^3 \left(\frac{\partial p_{x_i}}{\partial x_i} \right) \quad [9]$$

in which k and $k + 1$ are two successive iteration steps. Initial values of p_c can be generated by a simple integrating scheme and the boundary condition stated in Eq. [5] should be observed throughout the iterative process. The completion of this iterative process is determined by the absolute difference between two successive iteration steps. It terminates if this difference is less than a pre-defined threshold.

EXPERIMENTAL SETUP AND RESULTS

In Vitro Flow Phantom Validation

Before applying the above process to *in vivo* studies, two *in vitro* experiments were performed to provide appropriate validation of the proposed technique. The first one consisted of an open-topped rotating cylinder containing water, as illustrated in Fig. 1a. The steady angular velocity of the cylinder was controlled by a high precision rotary motor, and the fluid within had reached hydraulic equilibrium (*solid body rotation*). In this case, the pres-

sure value at any given point within the fluid should be proportional to its vertical distance below the surface. In other words, if we measure the pressure distribution within a horizontal cross section of the cylinder, the result expressed in millimeters of water (mm H₂O) should match the surface shape of the fluid. This relationship was used to evaluate the accuracy of our proposed numerical method. Figure 1b, shows the calculated relative pressure distribution within the image plane, and Fig. 1c shows the central horizontal pressure profile of the calculated result and its correlation with the surface shape of the fluid. An encouragingly close match was achieved. Slight discrepancies may reflect minor inaccuracies in the velocity data, particularly in voxels spanning the fluid boundary.

Although the rotating cylinder phantom provided a convenient way of assessing pressure results calculated from MR data, it should be noted that its velocity field, and hence the calculation, involved spatial but not temporal acceleration. As the fluid had reached hydraulic equilibrium, i.e., $\partial u_i / \partial t = 0$, transient inertia played no part in balancing Eq. [1]. We therefore devised a phantom with transient motion. It consisted of a glass tank filled with water in which a relatively large scale standing wave was induced, as shown in Fig. 2. A pivoted flap, located at an antinode of the wave approximately a quarter wavelength from one end of the tank and driven by a motor located outside of the magnet, was used to generate wave motion. By preliminary testing, the natural frequency of the single standing wave, and a readily achieved wave amplitude were determined, were recorded, and were reproduced in subsequent experiments in and out of the magnet. Because the total length of the tank exceeded the extent of linearity of magnetic field gradients in the z direction, there was spatial displacement of image data close to each end of the tank. This artifact did not affect data in the central 30-cm field, which were used for analysis. A gating circuit was attached to the arm of the motor to allow for interleaved data acquisition similar to that of *in vivo* studies. A total of 24 time frames were collected for each cycle, the time interval between frames being 35 ms.

Figures 3a–3d show the calculated pressure at four different time instances positioned at 105, 245, 385, and 525 ms after the onset of the gating pulse. Within each subfigure, the top picture shows the overall pressure distribution with white for high pressure and black for low pressure. In the bottom subfigure, the pressure values are wrapped around at 1 mm Hg intervals, each occupying a complete gray scale range, so that a semi-quantitative visual assessment can be made. In this display scheme, the pressure gradient is proportional to the number of 1 mm Hg bands crossed in a given spatial distance.

During the calculations, the viscous terms in Eq. [1] were neglected, and this is justified as follows. The thickness of the unsteady viscous (Stokes) boundary layer in the fluid in contact with the wall may be estimated from the result of Stokes' second problem (10). This refers to the boundary layer above a harmonically oscillating plate, but a fluid oscillating parallel to a stationary plate is equivalent, and it results from an exact solution of the

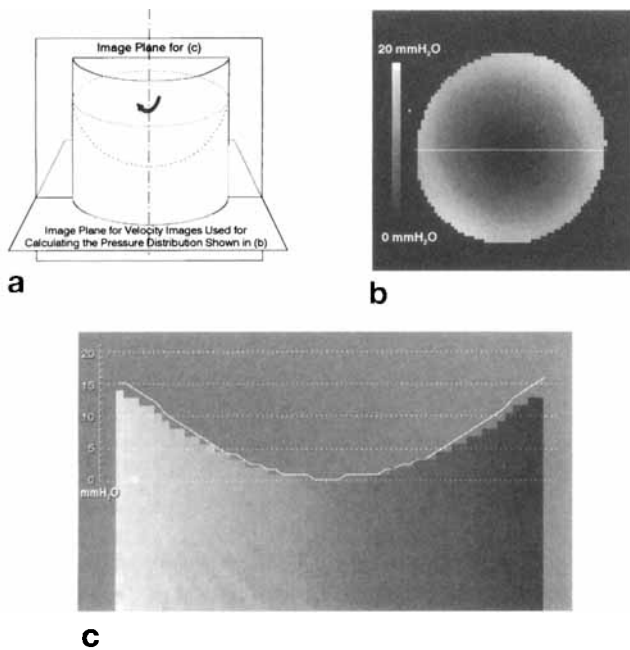


FIG. 1. (a) Schematic drawing of a phantom that contains water in a steadily rotating open-topped cylinder. (b) The calculated relative pressure distribution expressed in millimeters of water (mm H₂O) within a horizontal image plane as shown in Fig. 1a. (c) The central horizontal pressure profile of Fig. 1b and its correlation with the surface shape of the fluid determined by a through-plane velocity encoded image aligned with the axis of the phantom. Because the fluid had reached hydraulic equilibrium, a match between the surface shape of the fluid and the pressure profile (expressed in mmH₂O) should be expected. The imaging field of view used for this experiment was 30 cm.

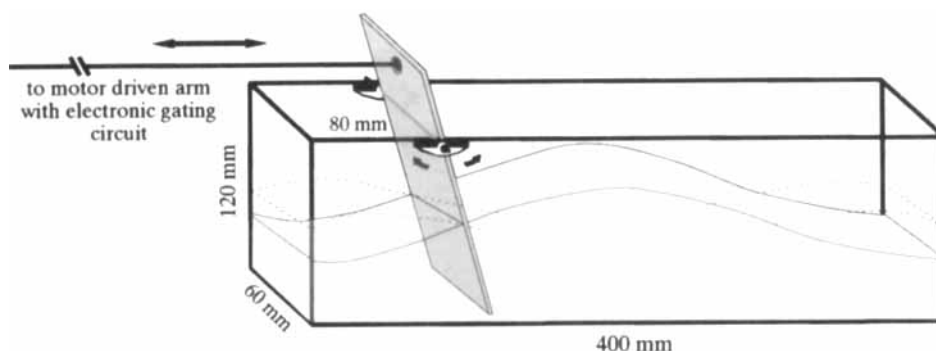


FIG. 2. A schematic diagram showing the configuration of the wave phantom. The glass tank is 400 mm in width, 120 mm in height, and 60 mm in depth. The water was filled to a level of 50 mm. A motor driven pivoted flap was used to generate large scale standing waves. A gating circuit was attached to the arm of the motor to allow acquisition of cine velocity data.

Navier-Stokes equation, which is valid for this case. The thickness of the layer depends on $\sqrt{\nu/\omega}$, in which ν is the kinematic viscosity of the fluid and ω the characteristic frequency. Boundary layers decay asymptotically with distance perpendicular to the wall, so thicknesses are defined arbitrarily. For pulsatile flow, they vary with time through the cycle; the fluid velocity is zero at the wall and reaches at least 99% of the undisturbed velocity when the distance from the wall is $8\sqrt{\nu/\omega}$. The frequency in the wave tank was approximately 1.7 Hz and, taking the kinematic viscosity of water as $0.01 \text{ cm}^2/\text{s}$, gives a boundary layer thickness of some 2 to 3 mm. Therefore, viscosity may be neglected over most of the depth of water in the tank. During image segmentation the boundary layer is excluded from the flow region Ω_F .

This neglect of viscous force is, in fact, advantageous for the numerical stability of the algorithm. The calculation of the viscous force involves taking the second-order derivatives of the original velocity data. This process is highly noise sensitive and may cause an undesirable effect on the accuracy of the pressure gradient, and this error will be propagated further during the final pressure calculation.

The actual pressures within the wave phantom were subsequently measured using a 2F Millar SPR-524 catheter-tip pressure transducer, which provides high-fidelity pressure readings. The transducer of the probe was set parallel to the main direction of fluid motion. Possible errors caused by deflection of the flow around the probe are likely to have been negligible, given the small size of the catheter and minute flow disturbance directed across its length.

Figure 4a shows the absolute temporal pressure variations measured at points A and B as marked in Fig. 3. In Fig. 4b, the temporal pressure difference between A and B is plotted as a solid line, whereas the corresponding pressure difference calculated from MR velocity data is delineated as a dotted line. Because these curves represent the pressure difference between two points, the unknown integration constant cancels out after subtraction. It can be seen that a good correspondence between the measured and calculated results was achieved. Some underestimation of the pressure difference, however, is evident for results derived from the MR velocity data. This can be attributed to a number of factors but the

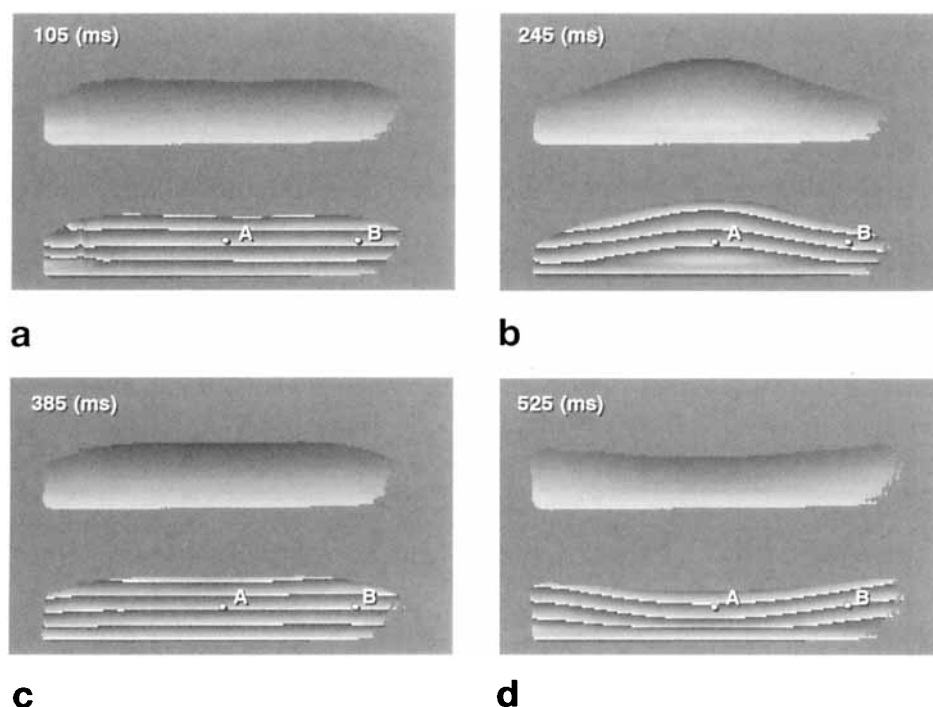
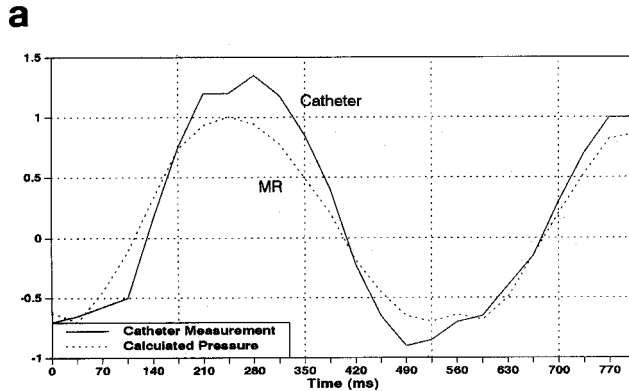
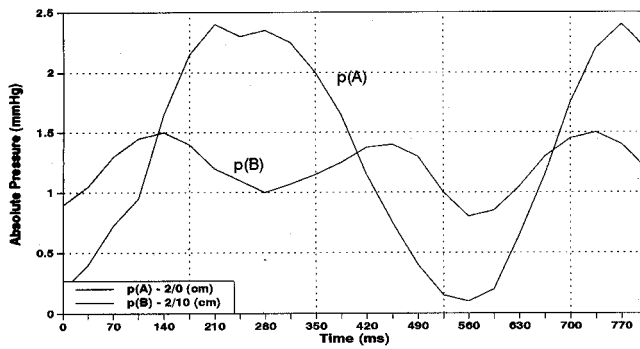


FIG. 3. The reconstructed pressure distribution for an *in vitro* flow phantom. The wave timed at (a) 105 ms, (b) 245 ms, (c) 385 ms, and (d) 525 ms after the onset of the electronic gating pulse. The top picture in each subfigure shows the overall pressure distribution with white for high pressure and black for low pressure. In the bottom subfigure the pressure values are wrapped around at 1 mm Hg intervals to provide a convenient visual assessment of pressure, pressure gradient, and isopressure contours. Catheter-tip pressure measurements were performed at positions marked as A and B, and the results were used to compare with MR measurements. Distortion of the wave tank outside the central 30-cm region of the field of view in image data was caused by nonlinearity of magnetic gradients.



b

FIG. 4. (a) The pressure measured at positions A and B of Fig. 3 using a high-fidelity catheter-tip pressure transducer. (b) A comparison of the pressure difference curves calculated from the catheter measurements (solid line) and that derived from the MR technique (dotted line).

following two are considered to be the primary causes:

1. The catheter measurement records the instantaneous pressure changes within the fluid, whereas the pressure calculated from the gated MR velocity data represents pressure variation derived from data acquired over many cycles. The averaging effect tends to smooth out small pressure fluctuations.
2. Although the time interval between successive frames was set to be 35 ms, this still may not be adequate for deriving temporal acceleration during peak acceleration or deceleration. Generally, the larger the time interval between successive sampling points, the more the underestimation of transient inertia, thus causing the rounding off of sharp pressure variations.

In Vivo Results

For illustration of *in vivo* application of the method described above we have chosen to analyze a study of blood flow velocity in the aortic arch of a healthy volunteer at rest (11). Figure 5 shows the time curve of mean flow velocity recorded in the ascending aorta. Solid circular markers indicate the times of calculated pressure distributions, which are to be shown in Figure 6. The position at which the mean flow velocity was measured is indicated by the arrow in Figure 6a. A total of 16 time frames

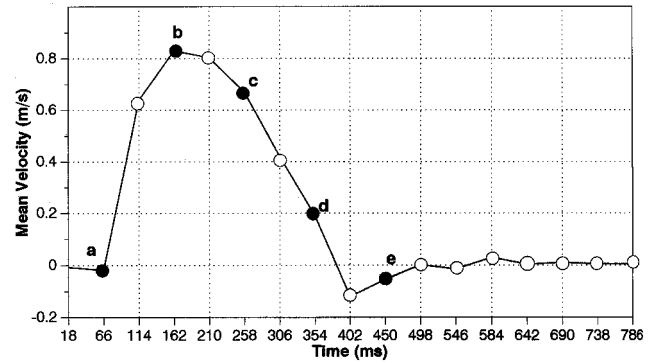


FIG. 5. The mean velocity in the ascending aorta measured at a position indicated by the arrow in Fig. 6a, with solid circular markers representing the time frames at which the pressure distributions were calculated. A total number of 16 time frames were acquired to cover evenly through systole and most of diastole. The time interval between slices was 48 ms.

were acquired to cover systole and most of diastole, and the time interval between frames was 48 ms. Acquisition was in a single slice aligned with the axis of the aortic arch.

Figures 6a–6e illustrate the calculated pressure distributions within the ascending/descending aorta timed at 66, 162, 258, 354, and 450 ms after the onset of the ECG R wave. To assist visualization, they have been superimposed on the magnitude images that show surrounding anatomic structures. The subject was studied in a supine position, and the force of gravity was neglected in our computation. As in the *in vitro* study, the top image of each subfigure shows the overall pressure distribution whereas the lower one uses 1 mm Hg pressure bands to provide a semi-quantitative representation of the pressure distribution.

In Figure 6, changing flow pressure gradients associated with pulsatile flow are apparent. The mass of fluid is almost at rest at the start of the cardiac cycle. In early systole (Fig. 6a), acceleration of blood is associated with a pressure gradient with relatively tightly packed 1 mm Hg pressure bands in the ascending aorta, and high pressure proximally. Toward peak systole, Fig. 6b, the driving pressure gradient declines, and by Fig. 6c, the direction of the gradient has started to reverse, retarding the blood flow. Maximum deceleration is evident in Fig. 6d, in which the higher pressure is located distally, in the descending aorta. It can also be seen that during peak flow, Fig. 6b, there is relatively high pressure toward the outer curvature of the aortic arch as a result of a centrifugal pressure gradient. At the end of systole, the aortic valve closes. The negative pressure gradient does not cause complete flow reversal, but restores flow to a steady state with almost zero velocity and a corresponding zero pressure gradient through diastole (Fig. 6e).

As with our wave tank study, the effects of viscosity were neglected. The Stokes layer in the aorta may be conveniently estimated from the Womersley parameter,

$$\alpha = \frac{D}{2} \sqrt{\left(\frac{\omega}{\nu}\right)}, \quad [10]$$

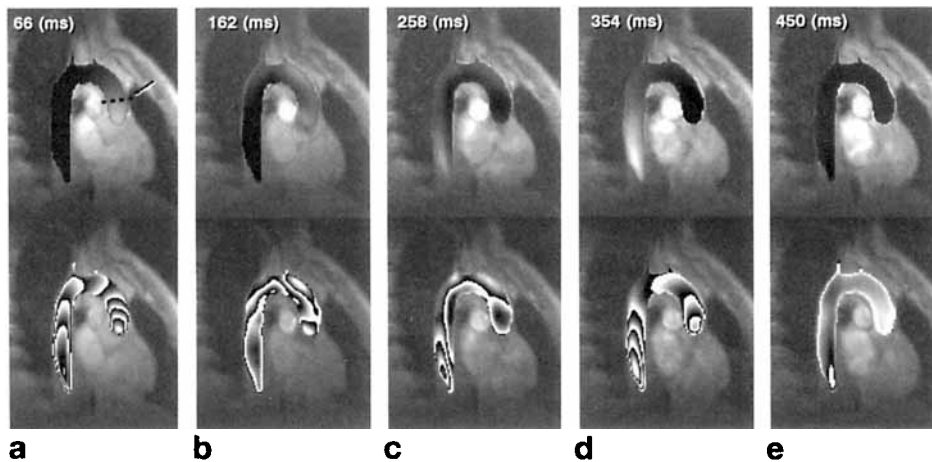


FIG. 6. The reconstructed pressure distribution for flow around the aortic arch. Five of sixteen time frames, corresponding to solid circular marker positions shown in Fig. 5, are displayed here. They illustrate pressure distributions at (a) 66 ms, (b) 162 ms, (c) 258 ms, (d) 354 ms, and (e) 450 ms after the onset of the ECG R wave. The top image of each subfigure shows the overall pressure distribution whereas the lower one uses 1 mm Hg pressure bands to provide a semi-quantitative representation of the pressure distribution.

with D being the blood vessel diameter. As mentioned earlier, ω is the characteristic frequency, and ν the kinematic viscosity of the fluid. The Womersley parameter represents the ratio of the radius of the pipe or artery to the unsteady boundary layer thickness. In this study, α was approximately 12.5 ($D \approx 2.0$ cm, pulsatile frequency ≈ 1 Hz, and assuming $\nu \approx 0.04$ cm²/s) so the boundary layer thickness was less than 1 mm; i.e., viscous effects are confined to a thin region near the wall.

DISCUSSION AND CONCLUSION

In this paper, we have presented an approach to the problem of computing flow pressure variations from MR velocity data. Our approach is based on use of the Navier-Stokes equations, which allow computation of pressure/flow relations in the region studied. Our aim was to map intravascular flow pressure distributions, contributing toward a better understanding of cardiovascular physiology and to provide a basis for investigation of abnormal blood flow dynamics. It must be emphasized that not absolute blood pressures but relative pressures within flow fields were sought by this technique. Conventional approaches to blood pressure measurement usually record pressure changes at limited locations without registering spatial variations of pressure. We have set out to visualize spatial distributions of flow pressure related to momentum changes. Altered distributions of flow pressure in the heart and great vessels are to be expected in a range of conditions, for example where there is impaired ventricular function, where there has been surgical reconstruction of the heart, and, in diseases such as atheroma, where there is altered compliance of arterial walls. The nature and significance of abnormal flow pressure distributions will require thorough investigation. This field of investigation should enhance understanding and clinical evaluation in a range of diseases of the heart and circulation.

There are, however, several limiting factors that should be considered. The multidirectional velocity mapping technique used has a relatively long data acquisition time, thus restricting the number of slices that can be imaged in a given time. This may be surmounted by using recently developed rapid volume flow imaging techniques (12) with improved spatio-temporal resolu-

tions. Also, attention should be paid to factors that affect the accuracy of the velocity phase mapping technique. These include partial volume averaging, misregistration effects, and phase errors introduced where there are higher orders of motion (13). Because transient inertia plays a dominant part in the Navier-Stokes equation, attempts are being made to reduce the time interval between successive image frames so that the smoothing effect described earlier can be minimized.

For the aortic arch study, acquisition of data in only one plane meant that any convective acceleration directed through the plane is overlooked. Our previous study of normal aortic flow (11) showed that the nonaxial component of velocity peaked at less than 30% of axial velocity and occurred during late systolic deceleration, during which transient rather than convective components of acceleration would dominate the balance of the Navier-Stokes equations. Through-plane convective acceleration can be expected therefore to play little part in the calculation of pressure gradients. Multiple plane or volume acquisition might be required, however, for the computation of flow pressure distributions in the presence of pathological distortions of the aorta.

In the present study, we have neglected viscous forces, and have given a justification for doing so. In the future, particularly if smaller blood vessels are to be investigated, it may be necessary to introduce the viscosity terms that we have omitted. There are further considerations that deserve attention. First, we have mentioned the problem of noise in the signal. One approach to dealing with this would be to smooth the data in a controlled way, probably using the continuity equation, which would impose internal consistency on the measurements and improve the results of subsequent analysis. A further problem is raised by the large time intervals between the cine frames, reducing the accuracy of the treatment of discretized equations involving time derivatives and integrations. This has made it difficult to relate pressure between time intervals, and we have been restricted to deriving differences of instantaneous pressure within the system. The possibility of reducing the time intervals has been mentioned. This would be particularly beneficial during phases of rapid change of momentum such as early systole. Further, suitable curve fitting procedures might be introduced to improve the

accuracy of arithmetic operations involving time. Linking the spatial and temporal progression of the pressure wave via knowledge of its speed of propagation in the aorta has been used in the past for investigating ventricular contraction efficiency (14, 15), and we believe this should be investigated further in the present context.

In conclusion, our results show the potential suitability of the proposed method for providing information on flow pressure fields associated with blood momentum change in the heart and large vessels. We believe that this approach will provide important new information on cardiovascular physiology and pathophysiology.

ACKNOWLEDGMENTS

The authors thank their colleagues in the Magnetic Resonance Unit and the Department of Paediatrics of Royal Brompton Hospital for their advice and critical suggestions. In particular, we wish to thank Dr. R. R. Chaturvedi and Mr. P. A. White for their assistance with catheter pressure measurement, Drs. P. Burger and D. G. Gibson for their helpful comments, and Mr. R. L. Hughes for designing the electronic gating circuit for the wave phantom.

REFERENCES

1. L. Hatle, A. Brubakk, A. Tromsdal, B. Angelsen, Noninvasive assessment of pressure drop in mitral stenosis by Doppler ultrasound. *Br. Heart J.* **40**, 131–140 (1978).
2. C. Chen, L. Rodriguez, J. L. Guerrero, S. Marshall, R. A. Levine, A. E. Weyman, J. D. Thomas, Noninvasive estimation of the instantaneous first derivative of left ventricular pressure using continuous-wave Doppler echocardiography. *Circulation* **83**, 2101–2110 (1991).
3. R. A. Nishimura, A. J. Tajik, Determination of left-sided pressure gradients by utilizing Doppler aortic and mitral regurgitant signals: validation by simultaneous dual catheter and Doppler studies. *J. Am. Coll. Cardiol.* **11**, 317–332 (1988).
4. H. B. Xiao, X. Y. Jin, D. G. Gibson, Doppler reconstruction of left ventricular pressure from functional mitral regurgitation: potential importance of varying orifice geometry. *Br. Heart J.* **73**, 53–60 (1995).
5. Y. C. Fung, "Biodynamics: Circulation," Springer-Verlag, New York, 1984.
6. S. L. Sobolev, in "Partial differential equations of mathematical physics," Pergamon Press, Oxford, 1964.
7. S. M. Song, R. M. Leahy, D. P. Boyd, B. H. Brundage, S. Napel, Determining cardiac velocity fields and intraventricular pressure distribution from a sequence of ultrafast CT cardiac images. *IEEE Tran. Med. Imag.* **13**, 386–397 (1994).
8. R. Weinstock, in "Calculus of variations: With applications to physics and engineering," Dover Publications, New York, 1974.
9. E. Kreyszig, in "Advanced engineering mathematics," 7th ed, John Wiley and Sons, New York, 1993.
10. H. Schlichting, in "Boundary layer theory," 7th ed, McGraw Hill, New York, 1979.
11. P. J. Kilner, G. Z. Yang, R. H. Mohiaddin, D. N. Firmin, D. B. Longmore, Helical and retrograde secondary flow patterns in the aortic arch studied by three-directional magnetic resonance velocity mapping. *Circulation*, **88** (part 1), 2235–2247 (1993).
12. D. N. Firmin, P. D. Gatehouse, J. P. Konrad, G. Z. Yang, P. J. Kilner, D. B. Longmore, Rapid 7-dimensional imaging of pulsatile flow, in "Proc., Computers in Cardiology, London, 1993," p. 353–356.
13. D. N. Firmin, G. L. Naylor, P. J. Kilner, D. B. Longmore, The application of phase shifts in NMR for flow measurement. *Magn. Res. Med.* **14**, 230–241 (1990).
14. S. Senda, M. Sugawara, Y. Matsumoto, T. Kan, H. Matsuo, A noninvasive method of measuring Max (dp/dt) of the left ventricle by doppler echocardiography. *J. Biomechanical Engineering* **114**, 15–19 (1992).
15. S. N. Urchuk, D. B. Plewes, An MR method for non-invasive blood pressure measurement, in "Proc., SMRM, 12th Annual Meeting, New York, 1993," p. 149.